ACS SENSORS

pubs.acs.org/acssensors
Article

Exploring MOF-Derived CuO/rGO Heterostructures for Highly Efficient Room Temperature CO_2 Sensors

Toton Haldar, Jia-Wei Shiu, Ren-Xuan Yang, Wei-Qi Wang, Hsin-Ting Wu, Hsu-I Mao, Chin-Wen Chen,* and Chi-Hua Yu*

Cite This: *ACS Sens.* 2024, 9, 5856−5865

Read Online

ACCESS | Metrics & More | Article Recommendations | Supporting Information

ABSTRACT: In response to the urgent need for advanced climate change mitigation tools, this study introduces an innovative CO_2 gas sensor based on p-p-type heterostructures designed for effective operation at room temperature. This sensor represents a significant step forward, utilizing the synergistic effects of p-p heterojunctions to enhance the effective interfacial area, thereby improving sensitivity. The incorporation of CuO nanoparticles and rGO sheets also optimizes gas transport channels, enhancing the sensor's performance. Our CuO/rGO heterostructures, with 5 wt % rGO, have shown a notable maximum response of 39.6−500 ppm of CO_2 at 25 °C, and a low detection limit of 2 ppm, indicating their potential as high-performance, room-temperature CO_2 sensors. The prepared sensor demonstrates long-term stability, maintaining 98% of its initial performance over a 30-day period when tested at 1-day intervals. Additionally, the sensor remains stable under conditions of over 40% relative humidity. Furthermore, a first-principles study provides insights into the interaction mechanisms with CO_2 molecules, enhancing our understanding of the sensor's operation. This research contributes to the development of CO_2 monitoring solutions, offering a practical and cost-effective approach to environmental monitoring in the context of global climate change efforts.

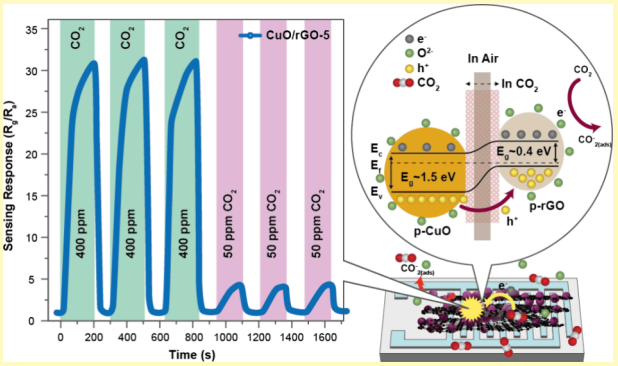

KEYWORDS: *metal organic framework, p-p heterojunction, graphene oxide, DFT, HOMO−LUMO energy gap*

Achieving carbon neutrality requires balancing emitted carbon with removal or offsetting, targeting net zero emissions to combat climate change.[1,2] Human activities like fossil fuel combustion and deforestation have significantly increased CO_2 levels, intensifying global warming.[3−5] Effective CO_2 detection is vital, enabling precise monitoring and management of greenhouse gases and informing reduction strategies. This necessitates the development of sensitive and economical gas sensors to address environmental and health risks.[6−9]

However, CO_2 significantly impacts indoor air quality by increasing concentrations of hazardous pollutants such as volatile organic compounds (VOCs), which can worsen health risks.[10,11] Elevated CO_2 levels enhance the greenhouse effect and deteriorate indoor environments, as shown in a 2021 study by Peng and Jimenez.[12] This study links high CO_2 levels to poor ventilation and potential pathogen transmission, including SARS-CoV-2.[12] In contrast, administering CO_2 under 300 ppm can promote plant growth by reducing microbial activity, while food storage areas may have CO_2 levels up to 25% to preserve freshness by inhibiting microbes.[13−15] This highlights the critical need for advanced room temperature CO_2 sensors for public health and specific applications such as agriculture and food preservation.

To enhance room-temperature gas sensing, a promising approach involves integrating metal oxides with higher electric charge carriers into reduced graphene oxide (rGO).[16,17] This technique prevents the aggregation of rGO sheets by enhancing electrostatically repulsive forces. Metal oxides such as ZnO, TiO_2, SnO_2, and WO_3, when combined with rGO and other 2D materials, form heterojunction materials that significantly improve the sensitivity of gas sensors.[18−22] For example, Kim et al.[23] developed a ZnO-graphene heterostructure CO_2 sensor, achieving a 78% response at 400 °C and a 1000 ppm detection limit. Amiri et al.,[24] enhanced CO_2 detection using graphene-TiO_2 nanocomposite layers (G-TiO_2−NCLs), achieving significant response improvements at 200 °C. Lee et al.[25] introduced a SnO_2-rGO nanocomposite sensor that demonstrated a strong linear response to CO_2 with a 5 ppm detection limit, offering low-cost and energy-efficient advantages. Tripathy et al.,[26] developed PEI/NrGO/ZNR

Received: June 11, 2024
Revised: August 14, 2024
Accepted: September 11, 2024
Published: September 18, 2024

https://doi.org/10.1021/acssensors.4c01397
ACS Sens. 2024, 9, 5856−5865

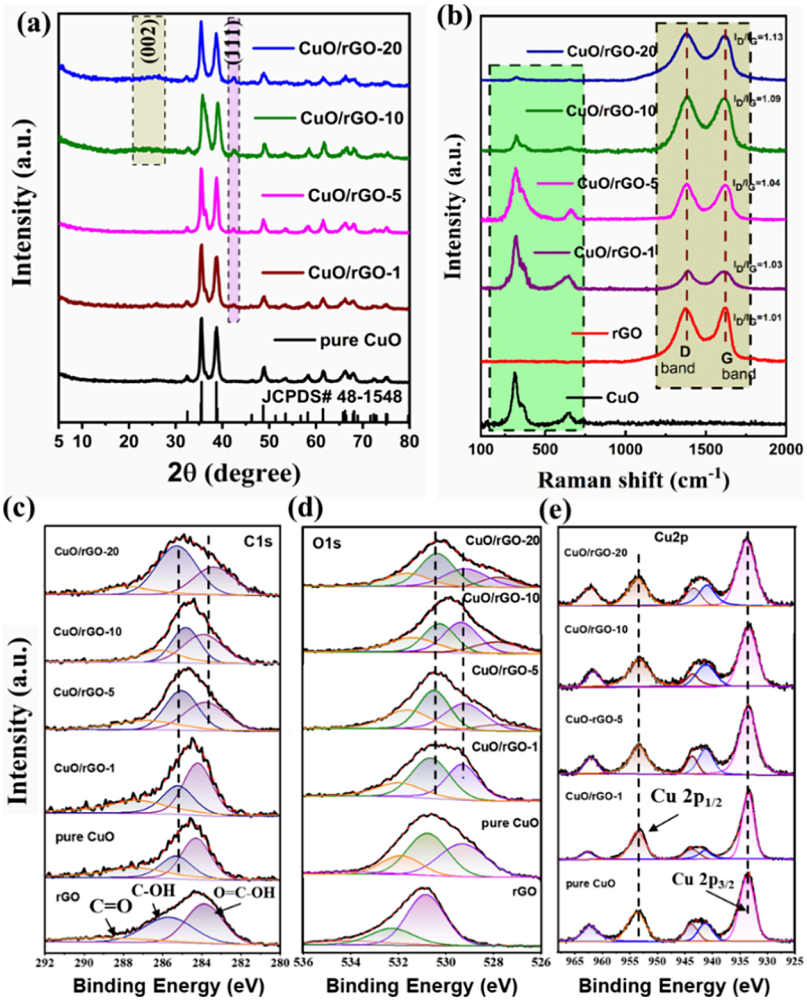

Figure 1. (a) XRD spectra of pure CuO, CuO/rGO-1, CuO/rGO-5, CuO/rGO-10, and CuO/rGO-20 heterostructures and (b) Raman spectra of pure CuO, GO, CuO/rGO-1, CuO/rGO-5, CuO/rGO-10, and CuO/rGO-20 heterostructures, XPS spectra of rGO, pure CuO, CuO/rGO-1, 5, 10, and 20 heterostructure composites (c) C 1s, (d) O 1s, and (e) Cu 2p.

sensors, showing a response increase from 5.6 to 16.98% with rising CO_2 levels, indicating potential for monitoring conditions like chronic obstructive pulmonary disease (COPD).

Copper oxide (CuO) is a p-type semiconductor with a band gap ranging from 1.2 to 1.9 eV, making it a versatile material suitable for various applications including catalysis, field emission devices, electrochemical cells, and gas sensors.[27,28] Meanwhile, metal−organic frameworks (MOFs), known for their adjustable topology and porosity through the selection of metal nodes and organic linkers, serve as excellent templates for creating various porous structures such as nanospheres, hierarchical flowers, and nanorods.[29−32] However, pure CuO gas sensors suffer from low sensitivity, a limitation often addressed by using MOFs as sacrificial templates to produce metal oxides and rGO with enhanced porosity and specific morphologies under controlled conditions.[33,34] Recently, this approach has become increasingly popular due to the advantageous properties of MOF-derived metal oxide, which enhance performance in sensor applications.[35,36] For example, Chen et al.,[37] utilized the MOF template to develop tourmaline@ZnO nanostructures, significantly enhancing n-butanol gas sensing by improving the surface area and electron transport efficiency. Similarly, Sun et al.,[38] demonstrate that Ce-doped In_2O_3 hollow nanoboxes derived from MOFs significantly enhance gas sensing, exhibiting rapid response and high sensitivity to formaldehyde.

In response to the critical need for advanced gas sensing technologies, particularly for the detection of CO_2 at room temperature, this study focuses on the development and evaluation of MOF-derived CuO/rGO heterostructures. Leveraging the novel combination of CuO, a metal oxide renowned for its gas sensing capabilities, with rGO, known for its exceptional properties and p-type semiconductor behavior, we aim to synthesize p-type heterostructures by using a simple solvothermal method. The objective is to harness the synergistic potential of CuO and rGO to enhance the gas sensing performance. Comprehensive characterization of these MOF-derived heterostructures will ascertain their physical and chemical attributes, crucial for their function as sensitive and selective CO_2 gas sensors. The study methodically evaluates the performance of these heterostructures as sensing materials, focusing on their sensitivity, selectivity, and response times to various gases, including CO_2, NH_3, CO, NO_2, H_2S, CH_4, and C_2H_5OH, across concentrations from 50 to 500 ppm. This encompasses a range of indoor and outdoor environmental scenarios. Additionally, density functional theory (DFT) analysis will be utilized to analyze the molecular interactions

https://doi.org/10.1021/acssensors.4c01397
ACS Sens. 2024, 9, 5856−5865

between the heterostructures and CO_2, enhancing our understanding of the detection mechanisms.

RESULTS AND DISCUSSION

Structure and Compositional Analysis. *X-ray Diffraction.* Solvothermally prepared CuO-MOF and CuO/rGO MOF powders were transformed into CuO/rGO heterostructures using a simple thermal decomposition methodology. The detailed experimental process is presented in the Supporting Information, as depicted in Figure S1. The crystalline structure of the synthesized pure CuO and CuO/rGO heterostructures, incorporating concentrations of 1, 5, 10, and 20 wt %, were recorded through powder X-ray diffraction (PXRD) analysis (Figure 1a). The PXRD patterns of pristine CuO resonated with the monoclinic-phase characteristics (JCPDS No. 45-1548), revealing peaks at 2θ values of 35.5° and 38.7°, which are emblematic of the $(11\bar{1})$ and (111) planes, respectively, thereby highlighting the crystalline integrity of CuO. Further, peaks positioned at 2θ angles of 32.4°, 46.3°, 48.6°, 51.2°, 53.6°, 58.9°, 61.6°, 66.3°, 68.2°, and 72.5° were ascribed to the monoclinic phase's (110), $(11\bar{2})$, $(20\bar{2})$, (112), (020), (202), $(31\bar{1})$, $(11\bar{3})$, (220), and (311) planes, respectively. The CuO/rGO heterostructures for the higher content of rGO (10 wt % of rGO and more) demonstrated a pronounced peak at 25°, attributable to the rGO peak. In contrast, for the lower content of rGO in CuO/rGO heterostructure (i.e., 1 and 5 wt % rGO), there were no detectable peaks for rGO. The absence of carbon-related diffraction peaks at ∼25° can be attributed to both the minimal presence and the low diffraction intensity of rGO.[39] Comparative diffraction spectra of CuO-BTC/rGO, graphene oxide (GO), and rGO substantiated the reduction of GO to rGO, facilitated by solvothermal treatment (Figure S2a,b). A distinct peak at ∼25° for 10 wt % and above CuO/rGO heterostructures (Figure 1a), denoted the graphene structure's disordered layer predominance, likely influenced by the differential rGO concentration, similar results were observed in the literature.[39,40]

Raman Analysis. Raman spectroscopy serves as a quintessential instrument for delving into the internal structural nuances of carbon-based composite materials. As illustrated in Figure 1b, the Raman spectral analysis encompassed pure CuO, GO, rGO, and CuO/rGO heterostructures with varying weight percentages. The characteristic D and G bands of carbon were discernible at approximately 1364 and 1605 cm^{-1}, respectively, across the spectra of GO, rGO, and CuO/rGO amalgamations (Figure 1b). Noteworthily, the I_D/I_G ratio, a quantitative marker of defect density within the Raman spectra of Cu/rGO, was observed to surpass that of pristine GO. This elevation signifies the reduction of GO to rGO via solvothermal processing, as evidenced in Table S1. The augmented I_D/I_G ratios within both composite formulations hint at an enhanced defect density, potentially stemming from the mild reducing effect of functional groups and the possible compromise of the sp^2 bonding network induced by the chemical interfacing between rGO and Cu. The I_D/I_G ratio for the solvothermally reduced rGO notably exceeded that of GO, indicating extensive damage to the carbon layer's crystal structure during the reduction process. This structural compromise fostered a proliferation of defects within the sp^2 lattice, elevating the structural disorder within the graphene matrix. The strategic incorporation of specific CuO concentrations into graphene, notably at 1, 5, 10, and 20 wt %, facilitated the amelioration of graphene's imperfections, as evidenced by a diminution in the I_D/I_G ratio. The Raman spectra delineated three distinct vibrational modes for both pure CuO and CuO/rGO-based heterostructures at approximately 298, 349, and 637 cm^{-1}, attributed to the Cu−O bond vibrations within the monoclinic CuO phase. An observable decrement in the vibrational frequencies' intensity, correlating with elevated rGO concentrations, suggests an augmented coverage of CuO nanoparticles by rGO sheets. The A_{1g} peak exhibited superior intensity relative to those of the B_{1g} and B_{2g} bands, indicating a pronounced crystallization of CuO, as corroborated by XRD analysis. This observation is in consonance with extant scholarly literature, thereby validating the experimental findings.[41]

X-ray Photoelectron Spectroscopy Analysis. Utilizing X-ray photoelectron spectroscopy (XPS), the valence states and surface compositions of the synthesized samples were meticulously examined. Presented in Figure 1c−e are the spectra for C 1s, O 1s, and Cu 2p corresponding to pure CuO, rGO, and the CuO/rGO composites designated as CuO/rGO-1, 5, 10, and 20. A comprehensive survey scan across all samples revealed the absence of impurities, as depicted in Figure S3. The calibration of all spectra was performed using the standard C 1s peak at 284.6 eV as a reference point. In Figure 1c, the deconvoluted C 1s spectra for both pure CuO and the CuO/rGO composites are displayed, illustrating peaks around ∼284.5, ∼286.8, and ∼288.9 eV. These peaks are indicative of the C−C, C−OH, and C═O groups, respectively, signifying the diverse carbonaceous environments present within the samples.[42] The CuO/rGO samples showed a decrease in the intensity of oxygen-containing groups compared with pristine rGO, indicating changes in surface chemistry following the hydrothermal treatment. Furthermore, Figure 1d presents a comparison of the O 1s XPS spectra for rGO, pure CuO, and CuO/rGO. The pure CuO, rGO, and CuO/rGO-1 spectra are deconvoluted into three distinct components representing O-related species centered at 533.8, 532.3, and 530.9 eV attributed to C═O, C−OH, and O═C−OH, for rGO and centered at 531.8, 530.7, 529.3 attribute to C−O, O−Cu, and C═O for CuO and CuO/rGO-1.[43,44] Whereas the higher content heterostructures show distinct components centered at 531.6, 530.29, 529.41, and 528.7 attributed to the C−O, O−Cu, O═C−OH, and C═O respectively. A noteworthy trend is the gradual diminution of oxygen vacancies with increasing graphene content, reaching a minimum at CuO/rGO-20. This trend suggests that the incorporation of graphene layers may influence the oxygen vacancy concentration, with the CuO/rGO samples exhibiting a higher prevalence of these vacancies than that of pure CuO. The increase in oxygen vacancies within the CuO/rGO heterostructures, as opposed to pristine CuO, is likely a consequence of the synergistic effects of rGO integration and the ensuing surface defect generation during the hydrothermal synthesis process. The enhanced gas sensing capabilities of the CuO/rGO heterostructures over pure CuO are ostensibly linked to the increased oxygen vacancy concentration within the former. This statement is further corroborated by the Cu 2p XPS spectra depicted in Figure 1e, where both CuO and CuO/rGO samples manifest the characteristic spectra of CuO. The binding energies identified at 933.2 eV for Cu $2p_{3/2}$ and 954.6 eV for Cu $2p_{1/2}$ are indicative of Cu(II) ions.[45] Additionally, satellite peaks at 943.0 and 962.6 eV affirm the

https://doi.org/10.1021/acssensors.4c01397
ACS Sens. 2024, 9, 5856−5865

existence of unfilled Cu 3d9 orbitals, reflective of Cu^{2+} in a paramagnetic chemical state.

Microstructural Analysis. *Surface Morphology.* The surface morphology of synthesized pure CuO, rGO, and the CuO/rGO heterostructure with 5% rGO content (CuO/rGO-5) was analyzed using field emission scanning electron microscopy (FE-SEM). This analysis highlighted the unique structural characteristics of each material. Figure 2a shows the

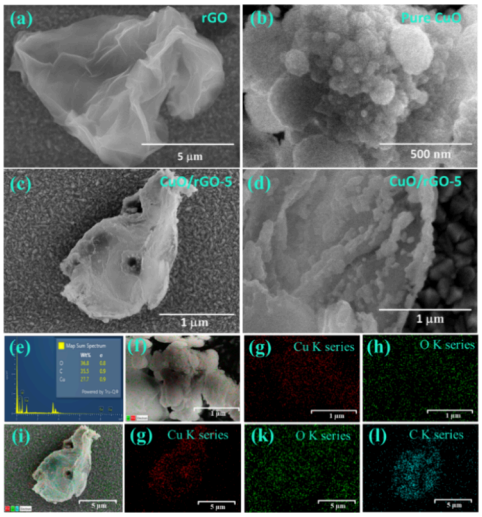

Figure 2. Field emission micrograph of (a) rGO, (b) pure CuO, (c,d) CuO/rGO-5 heterostructures, and (e) EDS elemental analysis of pure CuO (inset: EDS elemental spectra of CuO/rGO-5), (f–h) elemental mapping of Cu & O, and (i–l) CuO/rGO-5 elemental mapping of Cu, O, & C.

wrinkled, sheet-like structure of rGO, featuring visible 3–4 layers and slender edges. Figure 2b displays spherical CuO nanoparticles with a uniform size distribution. Figure 2c,d demonstrate a homogeneous dispersion of CuO nanoparticles across the rGO sheets. This uniform distribution potentially enhances the gas sensing properties of the composite by increasing both the active surface area and the number of heterojunctions between CuO and rGO. Figure 2e depicts the elemental compositions of CuO/rGO, focusing on elements such as Copper (Cu), Oxygen (O), and Carbon (C). For comparison, the elemental compositions of pure CuO are depicted in Figure S4. The energy dispersive spectroscopy (EDS) mapping, detailed in Figure 2f–l, provides deeper insight into the elemental distribution within the samples. The current elemental analysis of pure CuO and CuO/rGO heterostructures confirms that the prepared samples are free from impurities.

Transmission electron microscopy (TEM) and high-resolution TEM (HR-TEM) analyses of rGO, pure CuO, and CuO/rGO-5 heterostructures are presented in Figure 3. The TEM images of rGO show typical interconnected, sheet-like structures with a wrinkled surface and a clumped appearance as seen in Figure 3a. The low-loading rGO in the CuO/rGO-1 heterostructures displays agglomerates of very small, scattered nanoparticles, averaging 35 nm in size (Figure S5). In contrast, the higher rGO-based loading in the CuO/rGO-5 sample reveals a homogeneous distribution of smaller nanoparticles, averaging 30 nm, as shown in Figure 3c. Additionally, Figure 3d illustrates nanoparticles averaging 25 nm wrapped in a graphene sheet, alongside numerous tiny

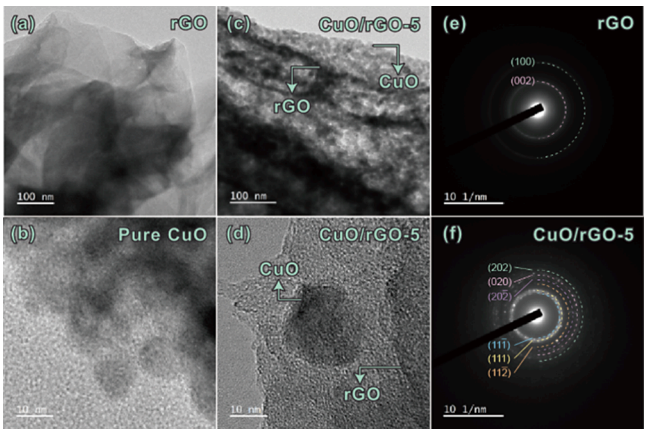

Figure 3. TEM micrograph of (a) rGO, (b) pure CuO, (c,d) TEM and HR-TEM of CuO/rGO-5 heterostructures, (e) SAED of rGO, and (f) SAED of CuO/rGO-5 heterostructures.

nanoparticles embedded within the graphene layers (Figure 3c). This dispersion highlights the ability of graphene sheets to support the growth of CuO nanoparticles in various shapes and sizes, fostering robust interconnected surfaces that develop through a synthesis process influenced by the dynamics of growth and dissolution. The selected area electron diffraction (SAED) patterns of rGO and CuO/rGO-5, depicted in Figure 3e,f, show rGO sheets as poly nanocrystalline in nature. The fringe spacing between the lattices measures 3.5 and 2.7 Å (Figure 3e), matching the *d*-spacing of the (002) and (100) reflection planes, respectively. Additionally, the continuous and diffused rings are indexed to the $(11\bar{1})$, (111), $(11\bar{2})$, $(20\bar{2})$, (020), and (202) planes of the monoclinic phase of CuO in the CuO/rGO-5 heterostructure.

Gas Sensing Performance. The critical role of operating temperature in the efficacy of gas sensing, particularly for metal-oxide semiconductor-based chemiresistors, is well-documented.[46,47] These sensors are known to exhibit temperature-dependent performance characteristics, including variations in response and recovery times. Consequently, an exploration was conducted to ascertain the optimal temperature range for CO_2 gas sensing, focusing on a span from 25 to 70 °C, with incremental adjustments of 5 °C (gas sensing experimental details are described in the Supplementary Information, a gas sensing experimental schematic is depicted in Figure S6). This investigation was illustrated in Figure 4a, which delineated the sensor response to 400 ppm of CO_2 across the specified temperature range for p-type heterostructure sensors. The findings highlighted a plateau in the sensor response commencing at 25 °C, establishing this as the optimal operating temperature for subsequent evaluations.

A peculiar decrease in the sensor response at 45 °C was observed, suggesting a modification in the CO_2 gas adsorption mechanisms. Further sensitivity tests at room temperature toward CO_2 concentrations ranging from 50 to 500 ppm were conducted on samples comprising pure CuO, rGO, and CuO/rGO heterostructures (with variations of 1, 5, 10, and 20 wt %) deposited over Interdigitated Electrodes (IDE). The dynamic response-recovery behavior of these samples to CO_2 is depicted in Figure S7. Notably, pure CuO sensors exhibited incremental responses to increasing CO_2 concentrations with a maximum response of 8.7% at 500 ppm. Conversely, pure rGO-based sensors showed negligible sensitivity to CO_2 at lower concentrations. The incorporation of rGO into CuO

https://doi.org/10.1021/acssensors.4c01397
ACS Sens. 2024, 9, 5856–5865

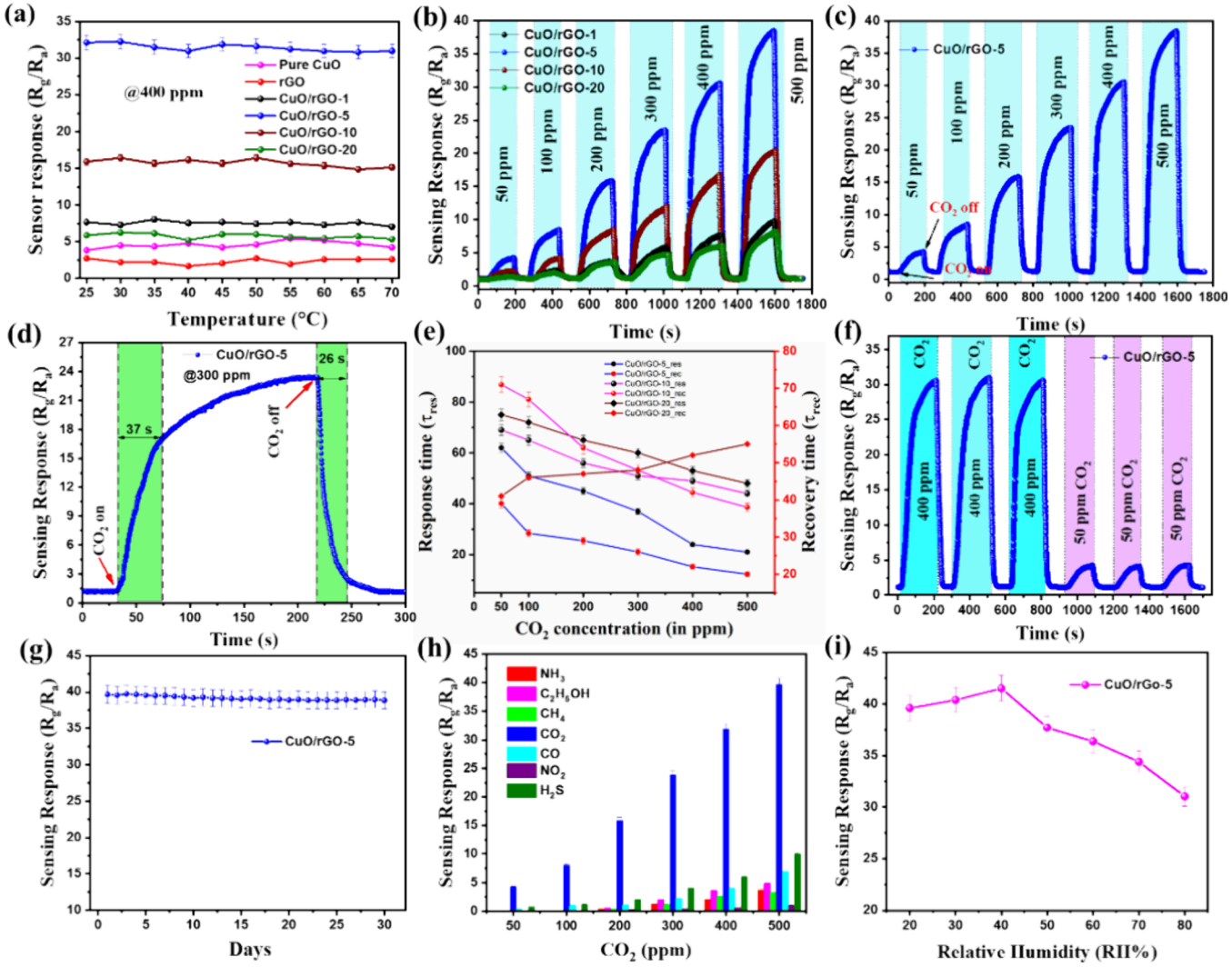

Figure 4. (a) Temperature-dependent CO_2 sensing response of all samples to 400 ppm of CO_2, (b) dynamic CO_2 sensing response-recovery curve of CuO/rGO-1, 5, 10, and 20, (c) dynamic resistance variation curves of the CuO/rGO-5 for different CO_2 content, (d) response and recovery curve of CuO/rGO-5 at 300 ppm of CO_2 content, (e) transient response/recovery curves of CuO/rGO-5, 10, and 20 heterostructures for different content of CO_2, (f) dynamic resistance variation curves of the CuO/rGO-5 at 400 and 50 ppm of CO_2, (g) long-term stability curve of the CuO/rGO-5 at 500 ppm of CO_2, (h) Selectivity bar diagram of all the samples for different analyte gases, (i) Humidity effect on the prepared CuO/rGO-5 CO_2 sensor.

significantly enhanced sensor responses, with the CuO/rGO nanocomposites demonstrating responses up to 39.6% at higher CO_2 levels (i.e., 500 ppm), marking a 10-fold increase in sensitivity compared to pure CuO sensors. This enhancement in sensor performance was most pronounced with a 5 wt % addition of rGO, beyond which the sensor efficiency gradually declined. The highest sensitivity of CuO/rGO-5 can be attributed to one of the reasons is 5 wt % rGO is an optimized concentration for creating the maximum number of heterojunctions between the metal-oxide and rGO. Additionally, higher concentrations of rGO may obscure the active surface area, leading to diminished sensing responses. This effect has been similarly observed in other rGO-based materials documented in the literature.[48,49]

The superior performance of CuO/rGO-5 heterostructures at room temperature underscores the potential of rGO incorporation in boosting gas sensing capabilities. Figures S7 further elucidate the sensors' dynamic sensing responses, illustrating a consistent rise in resistance with increasing CO_2 levels. This resistance trend, indicative of the sensors' operational characteristics, was systematically reported, affirming the CuO/rGO heterostructures' suitability for CO_2 detection in environmental and indoor settings. To gain a deeper understanding of the sensing behavior of the prepared sensors, we have included additional low-range sensor response curves for CuO/rGO-1, CuO/rGO-5, CuO/rGO-10, and CuO/rGO-20 samples exposed to 100 ppm of CO_2 in Figure S10a-d. These curves clearly illustrate the changes in response during gas exposure, highlighting both the increase and subsequent decrease in resistance. The sensing parameters of the prepared samples, tested under various CO_2 concentrations, are detailed in Table S2. Additionally, a comparative analysis of the CO_2 sensing performance related to our study is provided in Table S3. This analysis shows that the operational temperature of the CuO/rGO nanocomposite-based sensors is significantly lower compared with previously reported CO_2 gas sensors. For instance, Bhowmick et al.[50] reported a CuO/ZnO bilayer thin film for CO_2 detection that exhibited a higher

https://doi.org/10.1021/acssensors.4c01397
ACS Sens. 2024, 9, 5856−5865

sensor response but required an operating temperature of 375 °C. In contrast, our current CO_2 sensor achieves a comparable sensing response at room temperature. Thus, Table S3 briefly highlights the innovative advantage of this research in the development of efficient, low-temperature gas sensing technologies compared to recent reports.

The dynamics of response and recovery times are one of the key factors for assessing the effectiveness of gas sensors. Figure 4d depicts the response and recovery curve of the CuO/rGO-5 sensor to a 300 ppm of CO_2 concentration, with fast response and recovery times of 37 and 26 s, respectively. Further investigation into the response and recovery behaviors of CuO/rGO-5, CuO/rGO-10, and CuO/rGO-20 samples at various CO_2 concentrations is documented in Figure 4e, while the results for other samples are presented in Figure S8 and Table S2. Figure 4e concisely highlights the response and recovery times of the CuO/rGO material under ambient conditions, emphasizing its operational efficiency. The sensor's detection capabilities were evaluated, determining a Limit of Detection (LOD) for the present CO_2 sensor, based on a linear response-concentration relationship (Figure S9). The calculated LOD for the prepared CuO/rGO-5 sensor was 2 ppm. The LOD calculation, derived using the formula $3\sigma/m$, indicates a sensitivity that significantly exceeds both the Threshold Limit Values (TLVs) for CO_2 and typical human exhalation levels, marking a notable improvement in detection accuracy. The repeatability and stability of the CuO/rGO-5 sensors were confirmed through multiple sensing cycles, as depicted in Figure 4f. Consistent gas responses across three consecutive tests for 400 and 50 ppm of CO_2 concentrations highlight the sensor's excellent repeatability. A 30-day long-term stability test of the prepared CuO/rGO-5 showed minimal variation in the sensor response, within an experimental error margin of less than 1.9%, which is attributed to the stable oxidation states of the constituent layers, as illustrated in Figure 4g.

The selectivity of the CuO/rGO-5 sensor was tested by exposing it to various interfering gases, including CO, NH_3, H_2S, NO_2, CH_4, and CH_3OH, each at a concentration of 500 ppm and at room temperature. Figure 4h demonstrates the CuO/rGO-5 sensor's pronounced selectivity toward CO_2, a trait attributed to factors such as bond energy, gas molecular mass, and the specific morphology and crystal orientation of the gas-sensitive material. The prepared CuO/rGO-5 sensor exhibited significantly higher sensitivity to CO_2 over other gases like CO, H_2S, NO_2, CH_4, C_2H_5OH, and NH_3, and exhibited no response to N_2, highlighting its exceptional specificity. We also conducted additional experiments to examine the sensor response of CuO/rGO-5 samples to N_2, O_2, and a 50:50 mixture of the two gases at a concentration of 500 ppm (shown in Figure S11a–c). The findings revealed negligible sensitivity to both gases under the tested conditions, emphasizing the sensor's selectivity toward the target analytes (Figure S11a,b). However, a very low response was observed for the N_2/O_2 mixture (Figure S11c). The influence of humidity on gas sensing was also meticulously investigated, acknowledging its importance in the context of semiconducting sensor layers. Resistance measurements across a humidity range of 20–80 RH% revealed the nuanced impact of moisture on CO_2 sensing, as depicted in Figure 4i. The interaction between water molecules and ionized oxygen species, leading to electron donation and the formation of hydroxyl groups, elucidates the observed decrease in the sensor response at higher humidity levels. This suggests that while OH groups facilitate CO_2 adsorption on the metal oxide surface, effective CO_2 sensing also necessitates sites capable of electron donation. However, as humidity levels rise, the availability of such oxygen electron donors diminishes, indicating a need for an optimal humidity level for peak sensor performance, identified at 40% RH for 500 ppm of CO_2. This comprehensive examination of the CuO/rGO sensor's performance across various parameters response and recovery times, LOD, repeatability, selectivity, and humidity influence underscores its potential for enhanced CO_2 detection. Future research will delve into further optimizing sensor performance, particularly in reducing humidity cross-sensitivity, to refine detection limits and layer modifications.

Sensing Mechanisms. The functioning of a p-p-type heterojunction sensor is driven by the adsorption/desorption processes characteristic of a p-p-type metal oxide-semiconductor. As oxygen molecules are absorbed onto the grain surfaces, electrons are drawn from the valence band to these oxygen molecules. This electron transfer results in the formation of a hole-accumulation layer (HAL) on the surface.[51,52] The gas sensing mechanism of the present p-p type CuO/rGO heterostructures is comprehensively explained through the framework of conventional adsorption theory, as depicted in Figure 5. Prior research underscores that both pure CuO and rGO inherently possess p-type semiconductor properties.[53,54] This foundational premise guides the explanation that, upon exposure to air, oxygen molecules engage with these materials by capturing electrons, leading to the formation

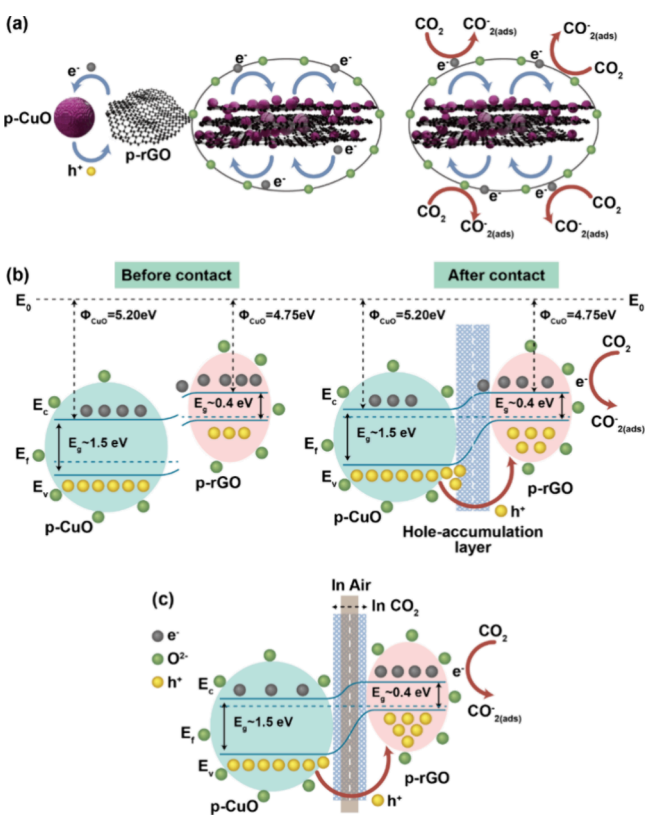

Figure 5. (a) Proposed schematic representation of the CO_2 gas sensing mechanism, (b) illustration of the formation of the p-p heterojunction of CuO and rGO, and (c) energy band diagram of CuO NPs combined with rGO.

https://doi.org/10.1021/acssensors.4c01397
ACS Sens. 2024, 9, 5856–5865

of chemically adsorbed oxygen ions on the material's surface, as illustrated in Figure 5a. Here, the monoclinic structure of CuO, characterized by its dangling bonds, exhibits a high catalytic activity for O_2 adsorption on its surface. PXRD reveals strong $(11\bar{1})$ and (111) peaks in the prepared polycrystalline CuO nanostructure, indicating a prominent presence of these planes on the CuO surface. This structure facilitates the formation of a large hole accumulation region on the CuO surface when exposed to an open atmosphere. Under ambient conditions, CO_2 serves as a reducing agent. The oxidization of CO_2 occurs via the negatively charged oxygen ions adsorbed on the surface, leading to electron release back into the material and the formation of $CO_2^-{}_{(ads)}$.[55] Consequently, as electrons and holes recombine, the hole concentration near the surface decreases, which in turn increases the device's resistance.

In other words, the cornerstone of these heterostructures' detection capability lies in the interaction between gas molecules and the adsorbed oxygen ions, which precipitates a change in the sensor's resistance. This interaction is underpinned by the chemical processes delineated in eqs 1 and 2, where oxygen molecules in their gaseous state $(O_{2(gas)})$ become adsorbed onto the surface $(O_{2(ads)})$ and subsequently capture an electron to form O^{2-} ions:

$$O_{2(gas)} \rightarrow O_{2(ads)} \tag{1}$$

$$O_{2(ads)} + e^- \rightarrow O_{2(ads)}^- \tag{2}$$

The gas sensing performance of CuO/rGO heterostructures is significantly enhanced by the formation of heterojunction interfaces between rGO and CuO. The CO_2 sensing mechanism in these heterostructures is influenced by the numerous small heterojunctions and the inherent chemical properties of both rGO and CuO. An increase in reactive sites, due to the rGO being decorated on the CuO, facilitates greater gas adsorption on the device's surface, resulting in an improved response to gas detection. Figure 5b illustrates the schematic representation of the p-p heterojunction formation, both pre- and postgas exposure. In these heterojunctions, the sensing response is primarily attributed to the CuO surface covered with rGO nanosheets, as depicted in Figure 5b. This is because there is a relatively smaller quantity of rGO on the CuO surface. The interplay between CuO nanoparticles and rGO, driven by their respective work functions CuO at approximately 4.75 eV and rGO around 5.20 eV facilitates the migration of holes from CuO to rGO and electrons in the converse direction until an equilibrium is established at both Fermi levels.

This p-p heterojunction formation, alongside modifications in the thickness of the hole accumulation layer at the heterojunction boundary, significantly contributes to the sensor's enhanced detecting capabilities, as showcased in Figure 5c. The charge transfer across the p-p junction, propelled by inherent electric fields, engenders a depletion layer, thereby augmenting the sensor's resistance and establishing potential barriers. In the presence of air, electrons ensnared by adsorbed oxygen augment the availability of holes near the surface. When encountering reducing CO_2 gas, the chemisorbed CO_2 escalates the number of available holes near the material's surface, thereby thickening the hole accumulation layer and further elevating resistance, as elucidated in Figure 5c.

The integration of rGO into CuO not only diminishes the electrical resistance when aired but also amplifies it upon CO_2 exposure. This phenomenon is attributed to the reaction between the O^{2-} ions and CO_2, leading to decomposition into CO_2^- and the release of electrons, responsible for the resistance increase, as outlined in eqs 3 and 4:

$$CO_2 + e^- \rightarrow CO_{2(ads)}^- \tag{3}$$

$$CO_2 + O_{2(ads)}^- + 2e^- \rightarrow CO_2^- + 2O^- \tag{4}$$

This process, wherein CO_2 gas molecule removal regenerates the charge carriers within the accumulation layer, culminates in a sensor resistance reduction, encapsulating the intricate interplay of reactions that underpin the gas sensing mechanism of the CuO/rGO heterostructures.

CONCLUSIONS

In conclusion, our study successfully synthesized CuO/rGO heterostructures derived from an MOF template using the solvothermal method. This investigation highlighted that the nanocomposites, characterized by the direct attachment of CuO nanoparticles to the 2D surface of graphene, undergo significant morphological and structural changes compared with their pure CuO and rGO counterparts. The p-p-type CuO/rGO heterostructures, especially those with a 5 wt % rGO composition, showcased superior gas sensing performance at ambient temperature. Notably, the sensing response of rGO-CuO-5 to 500 ppm of CO_2 was 39.6, which is 10-fold greater than that of pure CuO and 8-fold higher than that of rGO alone. Furthermore, the LOD for CO_2 was determined to be 2 ppm, based on linear regression analysis of the sensor response data.

The findings from density functional theory (DFT) calculations further elucidated the formation of p-p heterojunctions, underpinning the sensing mechanism proposed based on theoretical insights. The observed higher adsorption energy of the p-p heterostructure compared with other samples underscores its potential for developing a highly selective CO_2 gas sensor. This work not only advances our understanding of CuO/rGO heterostructures in gas sensing applications but also opens up new avenues for the design and optimization of sensitive and selective gas sensors for environmental monitoring and other critical applications. Such advancements hold great potential for improving indoor air quality and enhancing agricultural productivity, directly benefiting public health and sustainability.

ASSOCIATED CONTENT

Supporting Information

The Supporting Information is available free of charge at https://pubs.acs.org/doi/10.1021/acssensors.4c01397.

Experimental details on the solvothermal preparation of CuO-BTC and CuO/rGO, along with their schematic diagrams (Figure S1); detailed characterization techniques; XRD spectra for Cu(BTC), Cu(BTC)_rGO, GO, and rGO (Figure S2a,b); I_D/I_G ratios for GO, rGO, pure CuO, and CuO/rGO heterostructures at varying concentrations (CuO/rGO-1, CuO/rGO-5, CuO/rGO-10, CuO/rGO-20) (Table S1); survey scan XPS spectra for rGO, CuO, and the aforementioned CuO/rGO heterostructures (Figure S3); elemental compositions of pure CuO and rGO (Figure S4); TEM

https://doi.org/10.1021/acssensors.4c01397
ACS Sens. 2024, 9, 5856−5865

micrograph of CuO/rGO-1 (Figure S5); details on device fabrication and gas sensing measurements, including a schematic diagram of the gas sensing setup (Figure S6); dynamic resistance variation curves for the CuO/rGO series (Figure S7); dynamic response/recovery curves of pure CuO, rGO, and CuO/rGO-1 for different content of CO_2 (Figure S8); sensor responses at various CO_2 concentrations ranging from 50 to 500 ppm (Figure S9 and Table S2); different low-curve dynamic response data and selectivity study for N_2/O_2 (Figures S10 and S11); comparison of key CO_2 sensor parameters from earlier report (Table S3); and computational details and details analysis for theoretical calculations was described in details, with banddiagram and optimized structures in Figure S11 and Table S4 (PDF)

AUTHOR INFORMATION

Corresponding Authors

Chin-Wen Chen − *Department of Molecular Science and Engineering, National Taipei University of Technology, Taipei 106344, Taiwan;* orcid.org/0000-0001-6966-7573; Email: cwchen@ntut.edu.tw

Chi-Hua Yu − *Department of Engineering Science, National Cheng Kung University, Tainan 701401, Taiwan;* orcid.org/0000-0001-9445-3358; Email: jonnyyu@gs.ncku.edu.tw

Authors

Toton Haldar − *Department of Engineering Science, National Cheng Kung University, Tainan 701401, Taiwan;* orcid.org/0000-0003-2210-9990

Jia-Wei Shiu − *Department of Molecular Science and Engineering, National Taipei University of Technology, Taipei 106344, Taiwan*

Ren-Xuan Yang − *Institute of Environmental Engineering and Management, National Taipei University of Technology, Taipei 106344, Taiwan;* orcid.org/0000-0001-9589-629X

Wei-Qi Wang − *Department of Molecular Science and Engineering, National Taipei University of Technology, Taipei 106344, Taiwan*

Hsin-Ting Wu − *Department of Molecular Science and Engineering, National Taipei University of Technology, Taipei 106344, Taiwan*

Hsu-I Mao − *Department of Molecular Science and Engineering, National Taipei University of Technology, Taipei 106344, Taiwan*

Complete contact information is available at: https://pubs.acs.org/10.1021/acssensors.4c01397

Notes

The authors declare no competing financial interest.

ACKNOWLEDGMENTS

This study was conducted under the National Science and Technology Council (111-2314-B-006-047, 112-2314-B-006-011, and 113-2221-E-027-002) and was supported in part by Higher Education Sprout Project, Ministry of Education to the Headquarters of University Advancement at National Cheng Kung University (NCKU).

REFERENCES

(1) Qu, R.; Junge, K.; Beller, M. Hydrogenation of Carboxylic Acids, Esters, and Related Compounds over Heterogeneous Catalysts: A Step toward Sustainable and Carbon-Neutral Processes. *Chem. Rev.* **2023**, *123* (3), 1103−1165.

(2) Chapman, A.; Ertekin, E.; Kubota, M.; Nagao, A.; Bertsch, K.; Macadre, A.; Tsuchiyama, T.; Masamura, T.; Takaki, S.; Komoda, R.; Dadfarnia, M.; Somerday, B.; Staykov, A. T.; Sugimura, J.; Sawae, Y.; Morita, T.; Tanaka, H.; Yagi, K.; Niste, V.; Saravanan, P.; Onitsuka, S.; Yoon, K.-S.; Ogo, S.; Matsushima, T.; Tumen-Ulzii, G.; Klotz, D.; Nguyen, D. H.; Harrington, G.; Adachi, C.; Matsumoto, H.; Kwati, L.; Takahashi, Y.; Kosem, N.; Ishihara, T.; Yamauchi, M.; Saha, B. B.; Islam, M. A.; Miyawaki, J.; Sivasankaran, H.; Kohno, M.; Fujikawa, S.; Selyanchyn, R.; Tsuji, T.; Higashi, Y.; Kirchheim, R.; Sofronis, P. Achieving a Carbon Neutral Future through Advanced Functional Materials and Technologies. *Bull. Chem. Soc. Jpn.* **2022**, *95* (1), 73−103.

(3) Lashof, D. A.; Ahuja, D. R. Relative Contributions of Greenhouse Gas Emissions to Global Warming. *Nature* **1990**, *344* (6266), 529−531.

(4) Caldeira, K.; Jain, A. K.; Hoffert, M. I. Climate Sensitivity Uncertainty and the Need for Energy Without CO 2 Emission. *Science (80-.).* **2003**, *299* (5615), 2052−2054.

(5) Lelieveld, J.; Evans, J. S.; Fnais, M.; Giannadaki, D.; Pozzer, A. The Contribution of Outdoor Air Pollution Sources to Premature Mortality on a Global Scale. *Nature* **2015**, *525* (7569), 367−371.

(6) Hasan, D.; Lee, C. Hybrid Metamaterial Absorber Platform for Sensing of CO 2 Gas at Mid-IR. *Adv. Sci.* **2018**, *5* (5), No. 1700581.

(7) Tang, M.; Wang, Z.; Wang, D.; Mao, R.; Zhang, H.; Xu, W.; Yang, Z.; Zhang, D. Construction of LaF 3 QD-Modified SnS 2 Nanorod Composites for Ultrasensitive Detection of H 2 S. *J. Mater. Chem. A* **2023**, *11* (18), 9942−9954.

(8) Zhang, H.; Zhang, D.; Wang, Z.; Xi, G.; Mao, R.; Ma, Y.; Wang, D.; Tang, M.; Xu, Z.; Luan, H. Ultrastretchable, Self-Healing Conductive Hydrogel-Based Triboelectric Nanogenerators for Human−Computer Interaction. *ACS Appl. Mater. Interfaces* **2023**, *15* (4), 5128−5138.

(9) Wang, D.; Zhang, D.; Chen, X.; Zhang, H.; Tang, M.; Wang, J. Multifunctional Respiration-Driven Triboelectric Nanogenerator for Self-Powered Detection of Formaldehyde in Exhaled Gas and Respiratory Behavior. *Nano Energy* **2022**, *102*, No. 107711.

(10) Jacobson, T. A.; Kler, J. S.; Hernke, M. T.; Braun, R. K.; Meyer, K. C.; Funk, W. E. Direct Human Health Risks of Increased Atmospheric Carbon Dioxide. *Nat. Sustain.* **2019**, *2* (8), 691−701.

(11) López, L. R.; Dessì, P.; Cabrera-Codony, A.; Rocha-Melogno, L.; Kraakman, B.; Naddeo, V.; Balaguer, M. D.; Puig, S. CO2 in Indoor Environments: From Environmental and Health Risk to Potential Renewable Carbon Source. *Sci. Total Environ.* **2023**, *856*, No. 159088.

(12) Peng, Z.; Jimenez, J. L. Exhaled CO 2 as a COVID-19 Infection Risk Proxy for Different Indoor Environments and Activities. *Environ. Sci. Technol. Lett.* **2021**, *8* (5), 392−397.

(13) Zhang, X.; Wargocki, P.; Lian, Z. Human Responses to Carbon Dioxide, a Follow-up Study at Recommended Exposure Limits in Non-Industrial Environments. *Build. Environ.* **2016**, *100*, 162−171.

(14) Willits, D. H.; Peet, M. M. Predicting Yield Responses to Different Greenhouse CO2 Enrichment Schemes: Cucumbers and Tomatoes. *Agric. For. Meteorol.* **1989**, *44* (3−4), 275−293.

(15) Becker, C.; Kläring, H.-P. CO2 Enrichment Can Produce High Red Leaf Lettuce Yield While Increasing Most Flavonoid Glycoside and Some Caffeic Acid Derivative Concentrations. *Food Chem.* **2016**, *199*, 736−745.

(16) Geim, A. K.; Novoselov, K. S. The Rise of Graphene. *Nat. Mater.* **2007**, *6* (3), 183−191.

(17) Tan, C.; Cao, X.; Wu, X.-J.; He, Q.; Yang, J.; Zhang, X.; Chen, J.; Zhao, W.; Han, S.; Nam, G.-H.; Sindoro, M.; Zhang, H. Recent Advances in Ultrathin Two-Dimensional Nanomaterials. *Chem. Rev.* **2017**, *117* (9), 6225−6331.

(18) Ding, H.; Wei, Y.; Wu, Z.; Tao, K.; Ding, M.; Xie, X.; Wu, J. Recent Advances in Gas and Humidity Sensors Based on 3D Structured and Porous Graphene and Its Derivatives. *ACS Mater. Lett.* **2020**, *2* (11), 1381−1411.
(19) Tang, M.; Zhang, D.; Sun, Y.; Wang, Z.; Xi, G.; Chen, Q.; Mao, R.; Zhang, H. Chemiresistive Detection of SO2 in SF6 Decomposition Products Based on ZnO Nanorod/MoS2 Nanoflower Heterojunctions: Experimental and First-Principles Investigations. *Sensors Actuators B Chem.* **2024**, *403*, No. 135170.
(20) Zhang, D.; Yu, S.; Wang, X.; Huang, J.; Pan, W.; Zhang, J.; Meteku, B. E.; Zeng, J. UV Illumination-Enhanced Ultrasensitive Ammonia Gas Sensor Based on (001)TiO2/MXene Heterostructure for Food Spoilage Detection. *J. Hazard. Mater.* **2022**, *423*, No. 127160.
(21) Tang, M.; Zhang, D.; Chen, Q.; Wang, Z.; Wang, D.; Yang, Z.; Xu, W.; Wang, L.; Zhu, L.; An, F. Heterostructure Construction of SnS2 D Nanowires Modified with ZnO Nanorods for Chemiresistive H2S Detection in Sulfur Hexafluoride Decomposition Products. *Sensors Actuators B Chem.* **2023**, *390*, No. 133952.
(22) Zhang, H.; Chen, X.; Liu, Y.; Yang, C.; Liu, W.; Qi, M.; Zhang, D. PDMS Film-Based Flexible Pressure Sensor Array with Surface Protruding Structure for Human Motion Detection and Wrist Posture Recognition. *ACS Appl. Mater. Interfaces* **2024**, *16* (2), 2554−2563.
(23) Kim, J. S.; Kwon, S. Y.; Lee, J. Y.; Kim, S. D.; Kim, D. Y.; Kim, H.; Jang, N.; Wang, J.; Jung, D. G.; Lee, J.; Han, M.; Kong, S. H. ZnO/Graphene Heterostructure for Electrical Interaction and Application for CO 2 Gas Sensing. *Jpn. J. Appl. Phys.* **2023**, *62* (SG), SG1015.
(24) Amiri, M. T.; Ashkarran, A. A. Fabrication, Characterization and Enhanced Sensing Performance of Graphene-TiO2 Gas Sensor Device. *J. Mater. Sci. Mater. Electron.* **2017**, *28* (13), 9435−9441.
(25) Lee, Z. Y.; Hawari, H. F. bin; Djaswadi, G. W. bin; Kamarudin, K. A. Highly Sensitive Room Temperature CO2 Gas Sensor Based on SnO2-RGO Hybrid Composite. *Materials (Basel)* **2021**, *14* (3), 522.
(26) Tripathy, A. R.; Chang, C.; Gupta, S.; Anbalagan, A. K.; Lee, C.-H.; Li, S.-S.; Tai, N.-H. Polyethylenimine/Nitrogen-Doped Reduced Graphene Oxide/ZnO Nanorod Layered Composites for Carbon Dioxide Sensing at Room Temperature. *ACS Appl. Nano Mater.* **2022**, *5* (5), 6543−6554.
(27) Rahnama, A.; Gharagozlou, M. Preparation and Properties of Semiconductor CuO Nanoparticles via a Simple Precipitation Method at Different Reaction Temperatures. *Opt. Quantum Electron.* **2012**, *44* (6−7), 313−322.
(28) Zhang, Q.; Zhang, K.; Xu, D.; Yang, G.; Huang, H.; Nie, F.; Liu, C.; Yang, S. CuO Nanostructures: Synthesis, Characterization, Growth Mechanisms, Fundamental Properties, and Applications. *Prog. Mater. Sci.* **2014**, *60*, 208−337.
(29) Kong, L.; Yuan, Z.; Gao, H.; Meng, F. Recent Progress of Gas Sensors Based on Metal Oxide Composites Derived from Bimetallic Metal-Organic Frameworks. *TrAC Trends Anal. Chem.* **2023**, *166*, No. 117199.
(30) Garg, N.; Deep, A.; Sharma, A. L. Metal-Organic Frameworks Based Nanostructure Platforms for Chemo-Resistive Sensing of Gases. *Coord. Chem. Rev.* **2021**, *445*, No. 214073.
(31) Zhang, H.; Zhang, D.; Zhang, B.; Wang, D.; Tang, M. Wearable Pressure Sensor Array with Layer-by-Layer Assembled MXene Nanosheets/Ag Nanoflowers for Motion Monitoring and Human−Machine Interfaces. *ACS Appl. Mater. Interfaces* **2022**, *14* (43), 48907−48916.
(32) Wang, D.; Zhang, D.; Yang, Y.; Mi, Q.; Zhang, J.; Yu, L. Multifunctional Latex/Polytetrafluoroethylene-Based Triboelectric Nanogenerator for Self-Powered Organ-like MXene/Metal−Organic Framework-Derived CuO Nanohybrid Ammonia Sensor. *ACS Nano* **2021**, *15* (2), 2911−2919.
(33) Wang, D.; Chi, M.; Zhang, D.; Wu, D. Ammonia Sensing Properties of Metal−Organic Frameworks-Derived Zinc Oxide/Reduced Graphene Oxide Nanocomposite. *J. Mater. Sci. Mater. Electron.* **2020**, *31* (6), 4463−4472.
(34) Pan, Z.; Wang, D.; Zhang, D.; Yang, Y.; Yu, H.; Wang, T.; Dong, X. RGO Doped MOFs Derived α-Fe2O3 Nanomaterials for Self-Supporting Ppb-Level NO2 Gas Sensor. *Sensors Actuators B Chem.* **2024**, *405*, No. 135378.
(35) More, M. S.; Bodkhe, G. A.; Ingle, N. N.; Singh, F.; Tsai, M.-L.; Kim, M.; Shirsat, M. D. Metal-Organic Framework (MOF)/Reduced Graphene Oxide (RGO) Composite for High Performance CO Sensor. *Solid. State. Electron.* **2023**, *204*, No. 108638.
(36) Wang, D.; Zhang, D.; Pan, Q.; Wang, T.; Chen, F. Gas Sensing Performance of Carbon Monoxide Sensor Based on Rod-Shaped Tin Diselenide/MOFs Derived Zinc Oxide Polyhedron at Room Temperature. *Sensors Actuators B Chem.* **2022**, *371*, No. 132481.
(37) Chen, G.; Guo, Y.; Yang, X.; Li, G.; Yang, Z.; Huang, J.; Cheng, L.; Jiao, Z. MOF-Derived Tourmaline@ZnO Nanostructure as a High-Response Sensing Material of Gas Sensors toward n-Butanol. *ACS Appl. Nano Mater.* **2023**, *6* (12), 10725−10735.
(38) Sun, J.; Song, P.; Tian, Z.; Wang, Q. Ce-Doped Hollow In2O3 Nanoboxes Derived from Metal−Organic Frameworks with Excellent Formaldehyde-Sensing Performance. *J. Mater. Sci. Mater. Electron.* **2021**, *32* (23), 27290−27304.
(39) An, X.; Li, K.; Tang, J. Cu 2 O/Reduced Graphene Oxide Composites for the Photocatalytic Conversion of CO 2. *ChemSusChem* **2014**, *7* (4), 1086−1093.
(40) Lee, J. S.; You, K. H.; Park, C. B. Highly Photoactive, Low Bandgap TiO 2 Nanoparticles Wrapped by Graphene. *Adv. Mater.* **2012**, *24* (8), 1084−1088.
(41) Ranjbar-Azad, M.; Behpour, M. Facile in Situ Co-Precipitation Synthesis of CuO−NiO/RGO Nanocomposite for Lithium-Ion Battery Anodes. *J. Mater. Sci. Mater. Electron.* **2021**, *32* (13), 18043−18056.
(42) Chen, Y.; Zhao, S.; Wang, X.; Peng, Q.; Lin, R.; Wang, Y.; Shen, R.; Cao, X.; Zhang, L.; Zhou, G.; Li, J.; Xia, A.; Li, Y. Synergetic Integration of Cu 1.94 S−Zn x Cd 1−x S Heteronanorods for Enhanced Visible-Light-Driven Photocatalytic Hydrogen Production. *J. Am. Chem. Soc.* **2016**, *138* (13), 4286−4289.
(43) Boruban, C.; Esenturk, E. N. Activated Carbon-Supported CuO Nanoparticles: A Hybrid Material for Carbon Dioxide Adsorption. *J. Nanoparticle Res.* **2018**, *20* (3), 59.
(44) Teo, J. J.; Chang, Y.; Zeng, H. C. Fabrications of Hollow Nanocubes of Cu 2 O and Cu via Reductive Self-Assembly of CuO Nanocrystals. *Langmuir* **2006**, *22* (17), 7369−7377.
(45) Zhang, Q.; Huang, L.; Kang, S.; Yin, C.; Ma, Z.; Cui, L.; Wang, Y. CuO/Cu 2 O Nanowire Arrays Grafted by Reduced Graphene Oxide: Synthesis, Characterization, and Application in Photocatalytic Reduction of CO 2. *RSC Adv.* **2017**, *7* (69), 43642−43647.
(46) Tang, M.; Zhang, D.; Wang, D.; Deng, J.; Kong, D.; Zhang, H. Performance Prediction of 2D Vertically Stacked MoS2-WS2 Heterostructures Base on First-Principles Theory and Pearson Correlation Coefficient. *Appl. Surf. Sci.* **2022**, *596*, No. 153498.
(47) Tang, M.; Zhang, D.; Sun, Y.; Chen, Q.; Chen, Y.; Xi, G.; Wang, Z.; Shao, X. CVD-Fabricated Co3O4-Co3S4 Heterojunction for Ultra-Sensitive Detection of CO in SF6 Discharge Decomposition Products. *Sensors Actuators B Chem.* **2024**, *401*, No. 134968.
(48) Tammanoon, N.; Wisitsoraat, A.; Sriprachuabwong, C.; Phokharatkul, D.; Tuantranont, A.; Phanichphant, S.; Liewhiran, C. Ultrasensitive NO 2 Sensor Based on Ohmic Metal−Semiconductor Interfaces of Electrolytically Exfoliated Graphene/Flame-Spray-Made SnO 2 Nanoparticles Composite Operating at Low Temperatures. *ACS Appl. Mater. Interfaces* **2015**, *7* (43), 24338−24352.
(49) Qu, G.; Fan, G.; Zhou, M.; Rong, X.; Li, T.; Zhang, R.; Sun, J.; Chen, D. Graphene-Modified ZnO Nanostructures for Low-Temperature NO 2 Sensing. *ACS Omega* **2019**, *4* (2), 4221−4232.
(50) Bhowmick, T.; Ghosh, A.; Nag, S.; Majumder, S. B. Sensitive and Selective CO2 Gas Sensor Based on CuO/ZnO Bilayer Thin-Film Architecture. *J. Alloys Compd.* **2022**, *903*, No. 163871.
(51) Choi, S.-W.; Katoch, A.; Kim, J.-H.; Kim, S. S. Remarkable Improvement of Gas-Sensing Abilities in p-Type Oxide Nanowires by Local Modification of the Hole-Accumulation Layer. *ACS Appl. Mater. Interfaces* **2015**, *7* (1), 647−652.

https://doi.org/10.1021/acssensors.4c01397
ACS Sens. 2024, 9, 5856−5865

(52) Kim, H.-J.; Lee, J.-H. Highly Sensitive and Selective Gas Sensors Using P-Type Oxide Semiconductors: Overview. *Sensors Actuators B Chem.* **2014**, *192*, 607−627.
(53) Linnera, J.; Sansone, G.; Maschio, L.; Karttunen, A. J. Thermoelectric Properties of P-Type Cu 2 O, CuO, and NiO from Hybrid Density Functional Theory. *J. Phys. Chem. C* **2018**, *122* (27), 15180−15189.
(54) Mohd Shah, R.; Mohamad Yunus, R.; Mohd Shahbudin, M.; Minggu, L. J.; Wong, W. Y.; Mohd Nur, I. High Photoelectrochemical Performance of a P-type Reduced Graphene oxide-copper Oxide/Cu Foil (rGO-CuO/Cu) Photoelectrode Prepared by a One-pot Hydrothermal Method. *Int. J. Energy Res.* **2021**, *45* (9), 13865−13877.
(55) Sun, S.; Zhang, D.; Li, C.; Wang, Y. DFT Study on the Adsorption and Dissociation of H 2 S on CuO(111) Surface. *RSC Adv.* **2015**, *5* (28), 21806−21811.

https://doi.org/10.1021/acssensors.4c01397
ACS Sens. 2024, 9, 5856−5865